CrossMark

High-resolution Observations of Plume Footpoints in a Solar Coronal Hole

Kyung-Suk Cho[1,2] , Pankaj Kumar[3,4] , Il-Hyun Cho[5] , Maria S. Madjarska[6,7] , Valery M. Nakariakov[5,8] ,
Eun-Kyung Lim[1] , Wenda Cao[9,10] , Vasyl Yurchyshyn[9,10] , Xu Yang[9,10] , and Sung-Hong Park[1]
[1] Space Science Division, Korea Astronomy and Space Science Institute, Daejeon 305-348, Republic of Korea; kscho@kasi.re.kr
[2] Department of Astronomy and Space Science, University of Science and Technology, Daejeon 305-348, Republic of Korea
[3] Department of Physics, American University, Washington, DC 20016, USA
[4] Heliophysics Science Division, NASA Goddard Space Flight Center, Greenbelt, MD 20771, USA
[5] Kyung Hee University, Yongin-si, Gyeonggi-do 17104, Republic of Korea
[6] Max Planck Institute for Solar System Research, Justus-von-Liebig-Wig 3, D-37077, Göttingen, Germany
[7] Space Research and Technology Institute, Bulgarian Academy of Sciences, Acad. Georgy Bonchev St., Bl. 1, 1113, Sofia, Bulgaria
[8] University of Warwick, Coventry, CV4 7AL, UK
[9] Big Bear Solar Observatory, New Jersey Institute of Technology, Big Bear City, CA 92314, USA
[10] Center for Solar-Terrestrial Research, New Jersey Institute of Technology, 323 Martin Luther King Blvd., Newark, NJ 07102, USA

Abstract

Plumes are bright structures in coronal holes extending from the solar surface into the corona and are considered as a possible source of the solar wind. Plumes are thought to be rooted in strong unipolar photospheric flux patches (network/plage region). The magnetic activities at the base of plumes may play a crucial role in producing outflows and propagating disturbances (PDs). However, the role of photospheric/chromospheric activities (e.g., jets/spicules) at the base of plumes and their connection to PDs is poorly understood. Using high-resolution observations of a plume taken on 2020 July 23 with the 1.6 m Goode Solar Telescope (GST), Interface Region Imaging Spectrograph (IRIS), and the Atmospheric Imaging Assembly (AIA) on board the Solar Dynamics Observatory, we analyzed chromospheric/transition region activities at the base of the plume and their connection to outflows/PDs in the plume. The GST Visible Imaging Spectrometer images reveal repetitive spicules with blueshifted emission (pseudo-Doppler maps) at the plume's footpoint. In addition, the photospheric magnetograms provide evidence of mixed polarities at the base of the plume. The IRIS Mg II k Dopplergrams show strong blueshifted emission ($\sim$50 km s^{-1}) and a high brightness temperature (Mg II k2 line) at the footpoint of the plume. The long-period PDs ($P \approx$ 20–25 minutes) along the plume (AIA 171 Å) match the periodicity of spicules in the chromospheric images, suggesting a close connection between the spicules and the PDs. We suggest that the interchange reconnection between the closed and open flux of the coronal bright point at the plume's footpoint is the most likely candidate to produce upflows and associated PDs along the plume.

Unified Astronomy Thesaurus concepts: Solar coronal plumes (2039)

Supporting material: animations

1. Introduction

Plumes are hazy, ray-like open coronal structures expanding out to more than 30 $R_\odot$ (DeForest et al. 2001) and considered as a possible source for the solar wind (Poletto 2015). Plumes have been observed both in polar and equatorial coronal holes (Lamy et al. 1997; Raouafi & Stenborg 2014; Kumar et al. 2022). The lifetime of plumes ranges from 20 hr (Lamy et al. 1997) to two weeks (Withbroe et al. 1991) depending on the size of the plume. From earlier spectroscopic and imaging observations, the blueshifted plasma and propagating disturbances (PDs) in plumes are widely interpreted in terms of flows (e.g., Tian et al. 2011) and/or propagating slow-mode waves (e.g., Nakariakov 2006; Banerjee et al. 2011; Cho et al. 2021), but these interpretations remain under debate.

The formation mechanism of plumes is still unclear. According to the scenario proposed by Wang & Sheeley (1995), the emerging of bipoles from supergranular cells dragged by convection toward preexisting unipolar flux can produce a high-density flow collimated along open field lines via a magnetic reconnection process (Poletto 2015). Del Zanna et al. (2003) suggested that footpoint coronal bright points (CBPs; Madjarska 2019) of plumes can be seen only in the early phase of plume formation. Jets have been detected as a precursor prior to the appearance of plumes (Raouafi et al. 2007; Pucci et al. 2014). Raouafi & Stenborg (2014) suggested that plumes are formed and sustained by the dynamic evolution (tiny jets and bright points) at the plumes' footpoints resulting from episodic low-rate magnetic reconnection. However, it is still not clear whether jets and CBPs are essential for the generation of plumes. Cho et al. (2021) reported two types of plumes. One is denser, active plumes associated with CBPs, jets, and macrospicules at their base, and the other is a quasi-stable faint/diffuse plume without any significant activity at the base. Recent observations suggest that plumes are composed of several bright filamentary structures (so-called plumelets), which account for most of the plume's emissions (Uritsky et al. 2021). Recently, Kumar et al. (2022) discovered quasiperiodic brightenings ($T > 1$ MK) with a period of 3–5 minutes and associated jetlets at the base of four plumes located in equatorial/polar coronal holes (CHs) and suggested a possible role of the p-mode wave in triggering the episodic interchange reconnection at the chromospheric/transition region heights in the tiny null-point topologies at the base of

plumes. The quasiperiodic brightenings ($P \approx 5$ minutes) at the base of a plumelet correlate with extended jetlets and associated PDs. On the other hand, PDs of the EUV emission observed above sunspots have been associated with the leakage of 3 minutes of oscillation in the sunspot umbra (Tian et al. 2018). Thus, similar but longer-period PDs in plumes could also be linked with chromospheric oscillations.

Type II spicules could be one of the primary counterparts of the small-scale chromospheric features of the quiet plumes. From the Hinode (Kosugi et al. 2007) observations of the solar limb, it has been revealed that they are ubiquitously seen at the limb but fade away into the solar corona without a downward motion (de Pontieu et al. 2007). These spicules usually have a larger speed (50–150 km s^{-1}) and a shorter lifetime (10–150 s) than those of type I spicules. To explain the generation mechanism of type II spicules, two different views have been proposed. One view is that slow-mode shock waves and nonlinear Alfvén waves on vertical flux tubes could explain the formation of the spicules (Sterling 2000). The shock is generated by a pressure enhancement at a bright region and becomes stronger as it passes upward. The nonlinear torsional Alfvén wave could be produced by an unwinding motion propagating along the magnetic flux tube. The other view is that magnetic tension and/or magnetic reconnection drives type II spicules. For example, Martínez-Sykora et al. (2017) showed that amplified magnetic tension in the partially ionized chromosphere appears to generate spicules. The magnetic tension builds up from the interaction between the strong vertical magnetic flux concentration and the neighboring horizontal field and moves tangled magnetic fields above the solar surface through the ambipolar diffusion process. Samanta et al. (2019) suggested that spicules are generated by magnetic reconnection due to the presence of opposite-polarity magnetic flux around dominant-polarity magnetic concentrations. Although type II spicules have been proposed as a potential source of coronal heating and solar wind acceleration, this remains debatable.

It is generally accepted that plumes are associated with CBPs and jets from the network region. However, there are many issues related to plumes that are under discussion as pointed out by Poletto (2015). For example, Antonucci et al. (1997) reported that plumes have lower ion and electron temperatures than interplumes, indicating less heating in plumes than in the surrounding regions, which could be attributed to their enhanced masses. Thus, an association between plumes and jets as well as plumes and CBPs is not clear. In addition, the relationships between plumes and small-scale features at the base of the plumes are largely unexplored. For example, the link between plumes and type II spicules is still not clear. The formation and sustainability of the polar plumes are not well understood because in most cases the plume structures are overlapping with fore- and background emission structures.

As pointed out above, several unresolved issues concerning plumes may be due to the lack of high-resolution observations. The observations of the plume's footpoint are vital in understanding the relationship between different magnetic activities from the chromosphere to the corona. Here, we present a coordinated high-resolution observation of a CH plume using the Interface Region Imaging Spectrograph (IRIS; De Pontieu et al. 2014) and the Goode Solar Telescope (GST; Cao et al. 2010a) observations on 2020 July 23. Our main

observational targets are small-scale coronal features (or CBPs) at the base of the plume located in the northern polar CH.

In this paper, we investigate the relationship between spicule activities in the chromosphere and PDs in a polar plume. The following section describes the observations and the data processing. In Section 3, we present the analysis of chromospheric features located at the plume's footpoint, and their relationship with PDs in the plume. Finally, we summarize and discuss our results in Section 4.

2. Observations and Data Processing

We conducted a coordinated observation on 2020 July 23 by using the IRIS and GST at Big Bear Solar Observatory (BBSO). For an observation target, we considered plumes with a CBP near the base using observations from the Solar Dynamics Observatory (SDO; Pesnell et al. 2012)/Atmospheric Imaging Assembly (AIA; Lemen et al. 2012) 171, 304, and 193 Å images. The 3D noise-gating technique (DeForest 2017) was used to clean the AIA images.

To inspect the footpoint of the plume, we chose a plume located in the northern polar CH. We provided the pointing information of the plume for the IRIS observations. Once IRIS started to track the plume, GST followed the target with the IRIS pointing information.

Figure 1 shows the targeted plume located in the CH at ∼918″ (latitude) and ∼217″ (longitude). The dotted box indicates the field of view (FOV) of the GST observations. A coronal bright point was located near the base of the plume, as shown in the AIA 171 and 193 Å images. An SDO/AIA 171 Å animation reveals continuous outflows from the edge of the CBP from 15:00 to 18:00 UT.

IRIS observed the plume from 16:07 to 21:51 UT with 19 repeats of large sparse 64-step raster and 1400 Å slit-jaw images. The FOV of the slit-jaw image is 119″ by 119″, and the FOV for the raster is 63″ by 120″. We acquired the IRIS spectra in the near-ultraviolet (2783–2834 Å) and far-ultraviolet (1332–1358 Å and 1390–1406 Å) bands. The slit step and raster cadences are 16.9 s and 1084 s, respectively. We analyzed the Mg II k 2796 Å, C II 1336 Å, and Si IV 1403 Å line observations (the level 2 data) taken from 17:02:10 to 17:19:57 UT. The Mg II k3 and Mg II h3 (line cores) are formed in the upper chromosphere, and the peaks Mg II k2v and Mg II k2r are sensitive to the emission from the middle chromosphere. Note that the formation height difference between Mg II k3 and Mg II h3 is about 50 km (Pereira et al. 2013), and the height difference between Mg II k2 and Mg II h2 is about 350 km (Leenaarts et al. 2013).

We used the Mg II h and k line profiles for the temperature estimation and line-of-sight (LOS) blue–red (B–R) asymmetry in the chromosphere. According to Leenaarts et al. (2013), the Mg II k2 profile features can be converted to the brightness temperature at their $\tau = 1$ heights, since the source function is coupled with the local thermal conditions. There is a positive correlation between Mg II k2 average peak intensity and temperature of the middle chromosphere. This relationship has been confirmed by using the observed temperature obtained by the inversion of the Mg II line (Gošić et al. 2016) and numerical simulations (Leenaarts et al. 2013). In addition, Gošić et al. (2016) showed a good relationship between the temperature at the middle chromosphere and the average intensity of the Mg II k2 peak ($\frac{k2v + k2r}{2}$). Thus, we adopt the Mg II k2 average peak intensity as a proxy of temperature
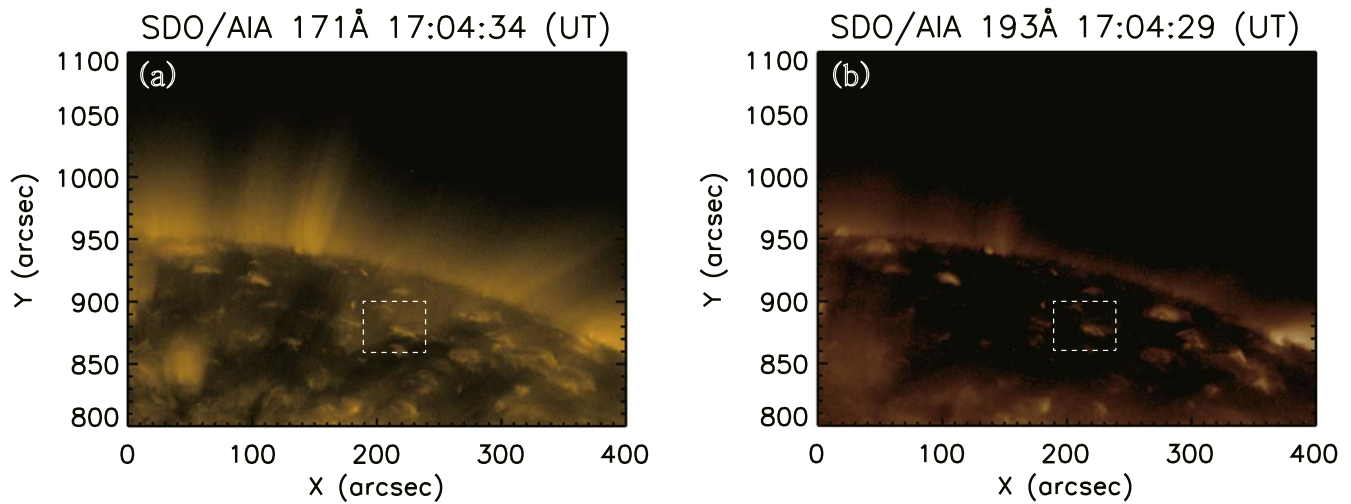
Figure 1. Small plume in a polar CH seen in SDO AIA 171 Å (a) and 193 Å (b). White dashed line boxes represent the FOVs of the Goode Solar Telescope (GST) at the Big Bear Solar Observatory (BBSO) and Interface Region Imaging Spectrograph (IRIS).

estimation in the middle chromosphere. More details about diagnostics based on the Mg II h and k lines can be found on the IRIS home page.[11]

We choose Mg II k line features to calculate LOS B–R asymmetry in the chromosphere because there is no significant difference in the $\tau = 1$ height differences between the Mg II k and Mg II h peaks. Owing to the Mg II profiles being double-peaked, it is not easy to apply a single Gaussian fit and the lambda meter method to the line profile. Instead, we adopt a method to determine the B–R asymmetry by subtracting the intensities (blue–red) at the symmetric velocity shifts from the line core. We carefully correct wavelength shifts by estimating wavelength shifts from the orbital velocity and thermal drifts. By applying the IRIS routine ("iris_prep _wavecorr_l2.pro") to each raster step, we obtain the shifts and subtract them from the wavelength scale. We then calculate a velocity scale for the Mg II k3 line and find the indices of the -50 and $+50$ km s^{-1} velocity positions. Finally, we produce a B–R asymmetry map that presents a difference between the intensities at two wavelength positions (± 0.5 Å, corresponding to ± 50 km s^{-1}) at the same distance from the Mg II k3 core. In the B–R asymmetry map, we use the convention of negative velocities for upflows. This procedure is also applied to C II 1336 Å and Si IV 1403 Å lines for the velocity comparison for the upper chromosphere and the transition region.

About 18 minutes after the start of IRIS observation, GST began to track the IRIS target with the aid of the adaptive optics (AO) system (Shumko et al. 2014). The seeing condition was good during the observation from 16:25 to 22:34 UT.

We selected the Broadband (10 Å) Filter Imager (BFI; Cao et al. 2010b), Visible Imaging Spectrometer (VIS; Cao et al. 2010a), and Near InfraRed Imaging Spectropolarimeter (NIRIS; Cao et al. 2012) installed at the GST. We acquired photospheric images every 15 s with a pixel scale of 0″034 from the BFI. The BFI was tuned on the TiO band (7057 Å) with 2.0 ms exposure time. In addition, chromospheric features at several wavelength positions from the Hα line center were obtained from the VIS, which provides narrowband (0.07 Å) images with a 70″ circular FOV. We obtained images at ± 0.8 Å (9 ms exposure time), ± 0.4 Å (15 ms exposure

time), and 0 Å (20 ms exposure time) from the Hα line center (6563 Å). The pixel scale of the obtained spectroscopic images is 0″029. Similar to the IRIS data analysis, we use pseudo-Dopplergrams (B–R asymmetry images) produced by subtracting Hα +0.4 and +0.8 Å intensities from -0.4 and -0.8 Å intensities, respectively.

Photospheric magnetic flux features were observed from 18:20 UT using the NIRIS with 63 s time cadence and 15 ms exposure time. We use a normalized Stokes V with Stokes I profiles for the LOS magnetic field information since NIRIS provides full Stokes I, Q, U, and V profiles at the Fe I 15648.5 Å. NIRIS has a circular FOV with 85″, and the scale resolution is about 0″08. To compare the magnetic features from NIRIS, we use SDO's Helioseismic and Magnetic Imager (HMI; Pesnell et al. 2012) magnetograms at 0″5 per pixel resolution. Finally, we obtained a speckle-reconstructed high-resolution TiO and VIS data set by using the Kiepenheuer-Institut Speckle Interferometry Package (Wöger et al. 2008).

Due to our observation with very small FOV ($<100''$) of the GST instruments, coalignment between GST images and IRIS requires a particular method. We use SDO/HMI data as a reference for the coalignment and apply the scale-invariant feature transform (SIFT) method to GST/TiO and SDO/HMI continuum data. We derived accurate image scale, FOV center, and FOV rotation angle information by comparing granulation structures from these images. This information is applied to all GST data, such as VIS and NIRIS. The detailed process for the accurate coalignment based on the SIFT method and its application to GST data sets is presented by Yang et al. (2022).

3. Results

Figure 2 shows the aligned SDO/AIA 171 Å, IRIS 1400 Å slit-jaw, SDO/HMI magnetogram, and NIRIS V/I images. Since the plume in the CH is very faint, the AIA 171 Å image in the figure is enhanced by subtracting smoothed images derived by averaging images obtained during 6 minutes prior to the event. From the enhanced image, we can identify a group of faint structures (i.e., plumes) as denoted by "A" in the AIA 171 Å image, which is also placed in the IRIS 1400 Å slit-jaw image. The IRIS 1400 Å image shows some strand (marked by "A") outflow features at the base of the plume. Although it
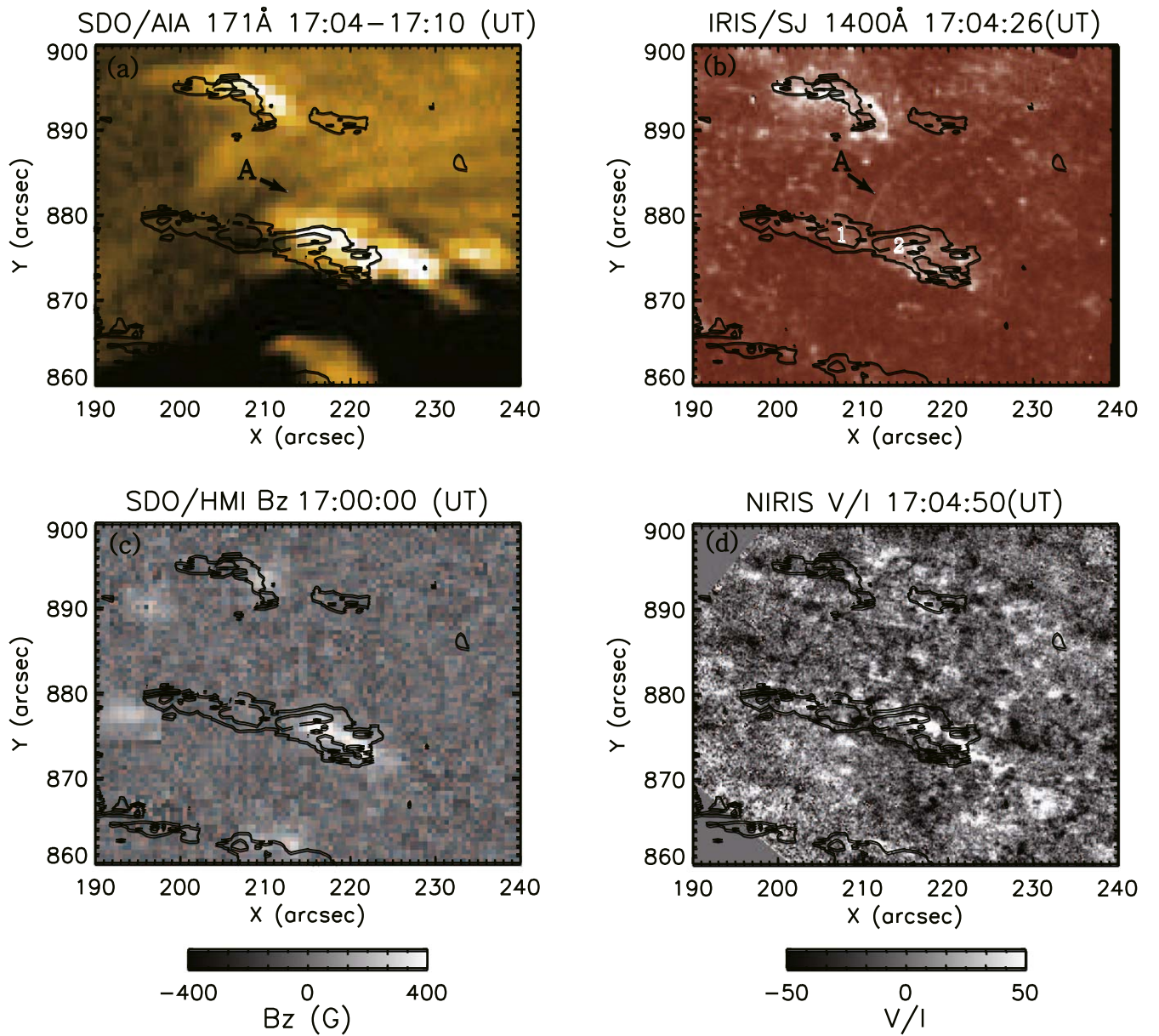
Figure 2. (a) Zoomed view of AIA 171 Å image, (b) IRIS/SJ 1400 Å image, (c) the vertical magnetic field (Bz) on the photosphere derived from SDO/HMI data, and (d) BBSO/NIRIS 10 minute averaged V/I within the white dotted line boxes in Figure 1. A faint plume (open structure) is marked by "A" in panels (a) and (b), and the contour levels (200 and 300) in these panels denote the brightness temperature obtained by the Mg II k2 line, in which the k2 average peak intensity is used as a proxy of temperature determination in the middle chromosphere. In panels (c) and (d), white and black colors represent positive and negative magnetic fields, respectively. An animation of this figure is available and the ranges of scaling for the HMI and NIRIS magnetograms are the same. The animation runs from 17:00:44 to 17:14:22 UT with a real-time duration of 7 s.

(An animation of this figure is available.)

appears that the arrow "A" points at different features, they are thought to be counterparts of the same feature since they are rooted in the same location and their evolution is synchronous. We speculate that the difference in appearance may be due to the different temperatures/regions that the two imaging channels sample ((a)—corona and (b)—transition region) combined with a projection effect as the region is inside a polar coronal hole. An SDO/HMI magnetogram reveals a majority polarity (positive) surrounded by background (opposite/negative) magnetic patches. An HMI animation from 15:00 to 18:00 UT shows no significant change (e.g., emergence or cancellation) in the magnetic flux as far as the polar data permit this to be seen. These tiny mixed polarities

(positive and negative patches) near the central positive polarity are better identified in the high-resolution averaged NIRIS V/I image (Figure 2(d)). To compare the locations of the plumes, we include a black contour representing the brightness temperature (Tb) obtained from the Mg II k2 average peak intensity, as described in the previous section. The Tb, a temperature proxy, has two separated peaks as denoted by "1" and "2" (Figure 2(b)). The plume's base is located at region 1 while region 2 corresponds to a CBP (see 171 Å image) rooted in a strong majority polarity (positive) near the base of the plume (Figure 2(b)).

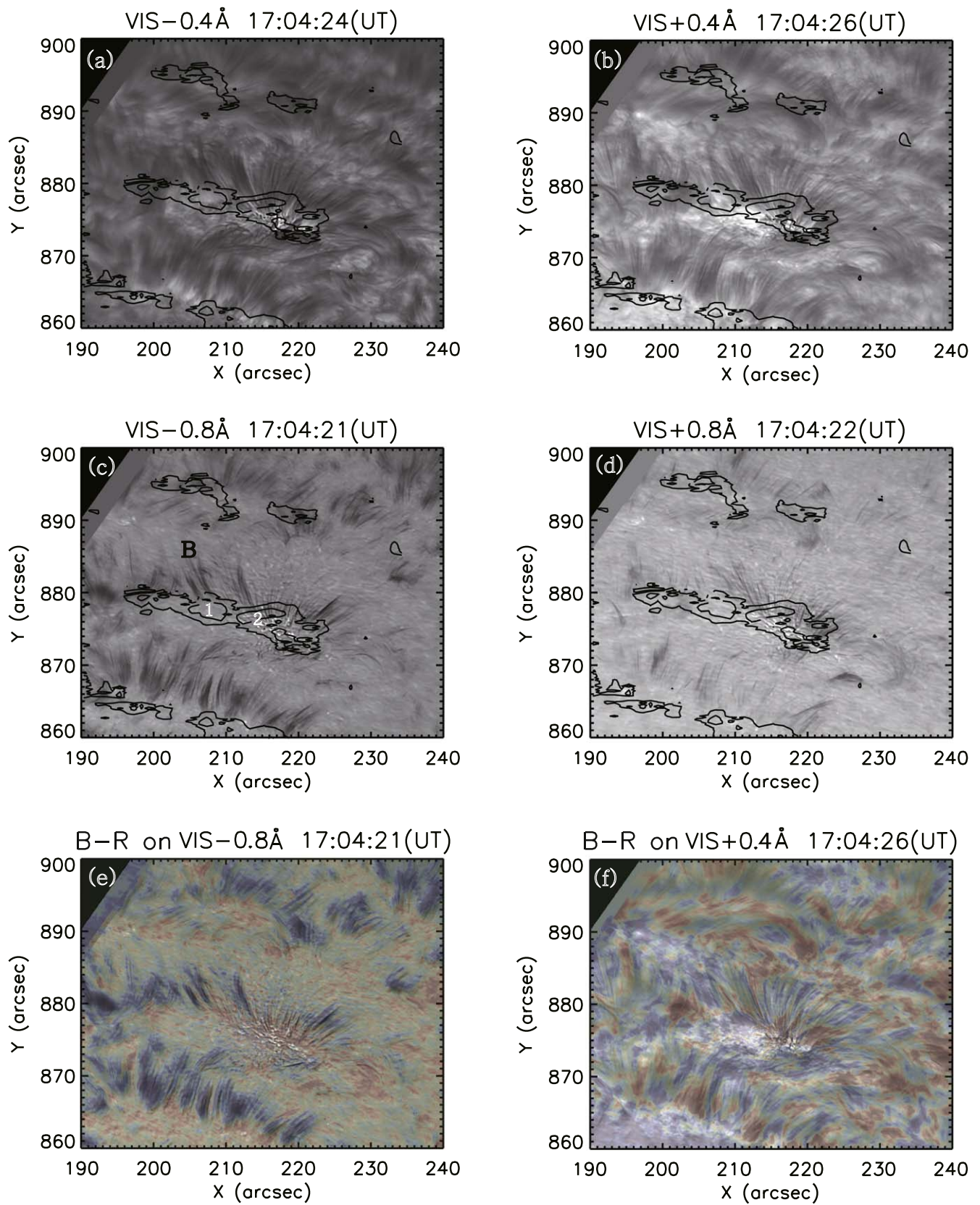We inspected the chromospheric features at the base of the plumes using the GST/VIS observations. Figure 3 shows

Figure 3. GST/Visual Imaging Spectrograph (VIS) observations of photosphere and chromosphere using Hα −0.4 Å (a), Hα +0.4 Å (b), Hα −0.8 Å (c), and Hα +0.8 Å (d). (e) and (f) are the Blue–Red subtracted images on the Hα −0.8 Å and the Hα +0.4 Å images, respectively. The locations of the spicules associated with the plume are denoted as "B" in panel (c). The contours represent high temperature networks deduced by the brightness temperature obtained by IRIS Mg II k2r and Mg II k2v lines observation. An animation of this figure is available online. The animation runs from 17:00:14 to 17:13:58 UT and its real-time duration is 6 s.

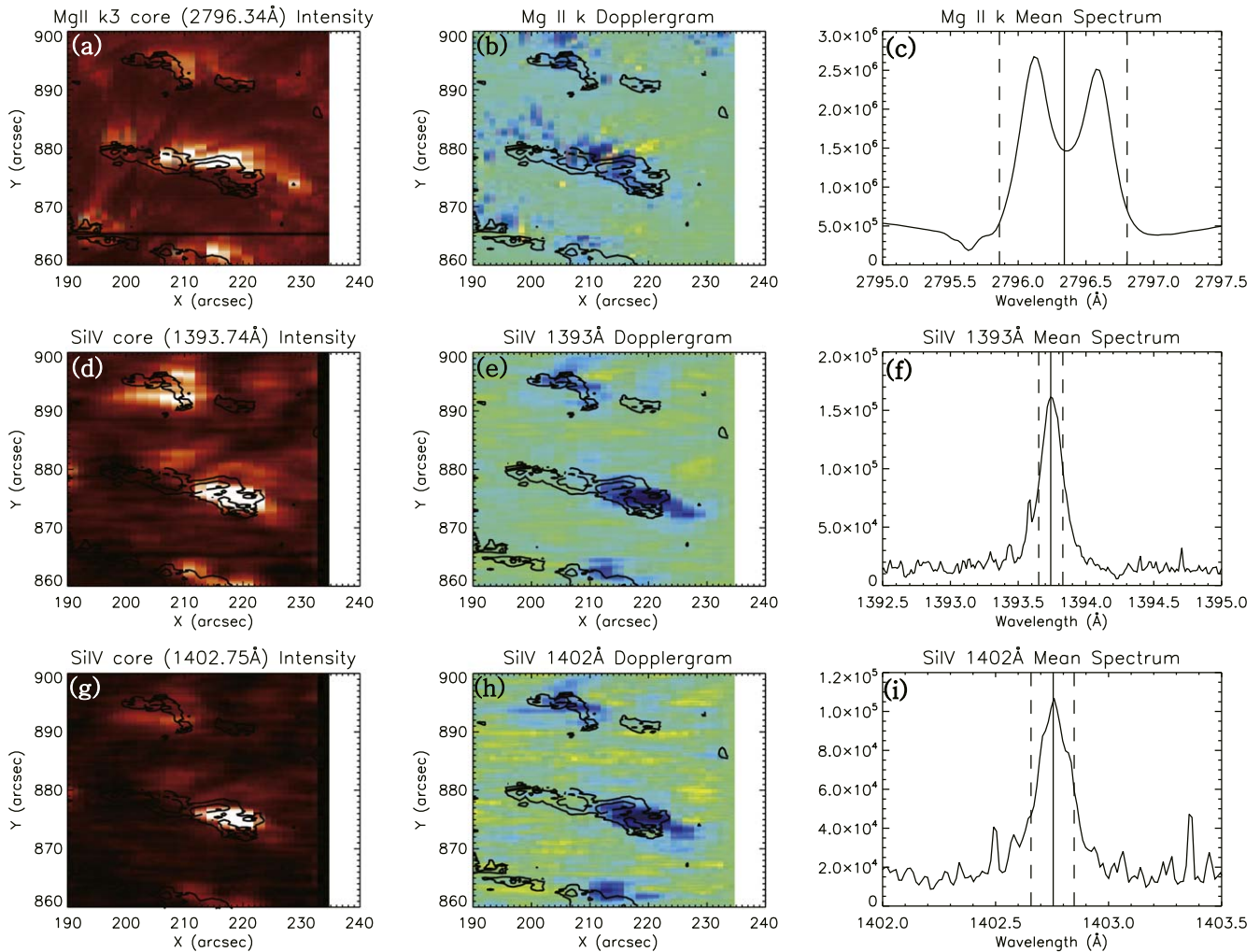(An animation of this figure is available.)

Figure 4. Line core images, Dopplergram (B–R asymmetry), and the spectra of IRIS Mg II k (upper panels), Si IV 1393 Å (middle panels), and Si IV 1403 Å (low panels). These spectra are averaged over a total area of about 45″ by 40″. The vertical solid line denotes the line core and dotted lines indicate two wavelength positions of the B–R asymmetries (± 50 km s^{-1} for Mg II k line and ± 20 km s^{-1} for Si IV and C II lines). The B–R asymmetry image is obtained from the intensity differences at the wavelength positions with the same distance from the line cores. Upflow (blue) features are identified from the chromosphere to the transition region.

dynamic chromosphere features from different off-band (with ± 0.4 Å and ± 0.8 Å offsets) images from the Hα line center on the Tb contour and the Doppler speed (blue–red subtraction) images. It is noteworthy that the chromosphere feature is the type II spicules because the spicules are more clearly seen in the blue (-0.8 Å) off-band, which are also known as rapid blueshifted excursions (RBEs). The RBEs are a cool component of type II spicules that show very rapid morphological changes with high-speed upflow motions. They are best seen in the blue wing of the Hα line. In addition, it is reported that their number seen in the FOV decreases with the increasing spectral line from 0.4 to 0.8 Å (Rouppe van der Voort et al. 2009; Yurchyshyn et al. 2020). Therefore, we chose H$\alpha \pm 0.8$ Å and H$\alpha \pm 0.4$ Å, which allow us not only to identify type II spicules without contamination by overlying type I spicules (fibrils) but also to extract Doppler velocities (blue–red subtraction) of the dark features from the pairs of spectral positions. As shown in Figure 3(c), type II spicules are rooted at the boundary of the Tb region, which may be related to magnetic reconnection taking place at the edge of the positive magnetic field concentration region interacting with neighboring small magnetic patches of opposite polarity. By

comparing the blue and red subtracted images seen in Figures 3(e) and (f), we can find that the spicules ("B") located in the Tb region "1" show strong upflow, and they are located at the footpoints of the plume.

In Figure 4, we present the IRIS raster scan observations. As shown in the left panels ((a), (d), and (g)), the line core emission in the Tb region, "1," is more clear in Mg II k3. In contrast, Si IV 1393 Å and Si IV 1403 Å line emissions are more substantial at the right side of region "2," indicating that they may come from different heights since Mg II is the chromospheric line and Si IV is the transition region line. It is noted that the Si IV lines have a higher formation temperature and the background emission in these lines is so strong that the weak emission from spicules cannot be distinguished. IRIS B–R asymmetry maps and the mean spectra in the FOV of the intensity maps are presented in the middle ((b), (e), and (h)) and right ((c), (f), and (i)) panels, respectively. These B–R asymmetry maps are obtained by using the intensity difference between blue and red off-bands at the two wavelength positions with the same distance from the line center, marked with vertical dotted lines in the right panels. To calculate the wavelength position, we estimate the velocity scale of each
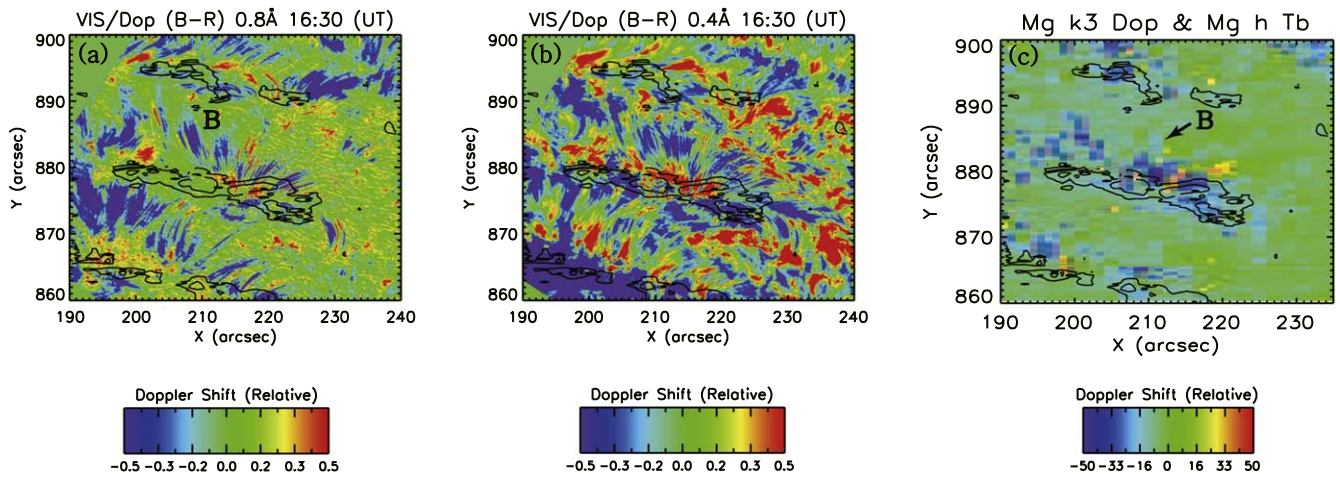
Figure 5. Pseudo-Doppler (B–R asymmetry) maps obtained by using GST/VIS Hα± 0.8 Å (a), GST/VIS Hα± 0.4 Å (b), and IRIS/Mg II k wing (c) intensities. Color bars present the upflows (blue) and downflows (red) with an arbitrary scale. An animation of the (a) and (b) panels is available. The animation shows the 17:00:11–17:13:54 UT sequence. The total real-time duration of the animation is 5 s.

(An animation of this figure is available.)

line. We use the velocity scale of $\pm 50\ \mathrm{km\ s^{-1}}$ for Mg II and $\pm 20\ \mathrm{km\ s^{-1}}$ for Si IV lines. We then find the indices of the corresponding velocity positions in the FOV and display the B–R asymmetry maps that are made using the instantaneous measurements in the middle panels ((b), (e), and (h)) using the convention of blue colors for upflows.

We applied a similar analysis technique to the VIS data for inspecting the line-of-sight velocity distribution at the chromosphere. Figure 5 shows the B–R asymmetry instantaneous maps determined by the intensity difference between blue and red off-bands of VIS data (left and middle panels), and Mg II data (right panel for comparison), in which the blue indicated the upflows and the solid contour lines denote the Tb. The Hα intensity images at ±0.8 Å and ±0.4 Å are used to calculate the B–R asymmetry maps. The B–R asymmetry maps from the ±0.8 Å and ±0.4 Å off-bands show upward (blue) and downward (red) moving chromospheric materials with speeds of $\sim 36\ \mathrm{km\ s^{-1}}$ and $\sim 18\ \mathrm{km\ s^{-1}}$, respectively. As denoted by "B" in panel (a), the type II spicule associated with the plume shows upflows in the lower chromosphere from Tb region "1" and the upflows are also identified in the middle chromosphere as shown in panels (b) and (c). It is found from the pseudo-Doppler (B–R asymmetry) animation that there are repetitive upflows from the spicules that are mostly rooted at the edges of the Tb region.

To investigate the possibility that type II spicules could be one of the sources of the plume, we compared the occurrence periods of the spicules and PDs in the plume. We apply the periodogram technique (Scargle 1982; Horne & Baliunas 1986; Nakariakov & King 2007) to the VIS B–R asymmetry map, and the AIA 171 Å and 304 Å intensity maps, respectively, and get the period information as shown in Figure 6. The top panels show the power maps of periodic change of AIA 171 Å intensity at three bands (5–10, 10–15, and 20–25 minutes). The short-period (5–10 minutes) power map is filled with noise, which is challenging for identifying any clear periodic pattern from the map. As the period increases, the plume features are revealed, as shown in the upper panels. We found that the plume structures extend out of the Tb region "1" on the long-period power map (20–25 minutes). The middle and bottom panels of Figure 6 represent the power maps of the occurrence

of type II spicules obtained by using AIA 304 Å and the VIS B–R asymmetry in the signals of the Hα ± 0.8 Å band, respectively. Similarly, the spicule features appeared clearly as the period increased. In general, long-period (20–25 minutes) power is located at the tips of the spicules, while the middle-period power is located at the roots of the spicules. Significantly, the Tb region "1" is more occupied with long-period power than the other areas. By comparing the long-period power maps from the AIA 171 and 304 Å intensity, and VIS B–R asymmetry, we find evidence that type II spicules at the footpoint of the plumes possibly supply energy to the plume with the extended periodic upflows. To investigate the magnetic activities at the footpoint of the plume, we created a time–distance (TD) intensity plot along the plume using AIA 171 Å images. The TD intensity plot along the slit (top panel of Figure 7) reveals repetitive brightenings (between $0''$ and $10''$) at the base of the plume and associated jetlets/PDs. We can derive the propagation speeds of the TDs by measuring their slopes on the middle panel of the figure. The estimated speeds from diagonal features are $160\ \mathrm{km\ s^{-1}}$ (left), $120\ \mathrm{km\ s^{-1}}$ (middle), and $106\ \mathrm{km\ s^{-1}}$ (right), respectively. Similar features have been detected by DeForest & Gurman (1998) and interpreted as slow magnetoacoustic (MA) waves. We also identify from typical spectra (as shown in the bottom panels of Figure 7) that intensity oscillations of the PDs at different distances at the positions "A," "B," and "C" have power peaks between 10 and 20 minutes corresponding to the MA waves. These results are also consistent with Jiao et al. (2015), who concluded that spicules are the primary source of PDs in plumes based on the AIA 171 and 304 Å observations. Since the evidence of magnetic reconnection is a potential novel point upon the studies of Jiao et al. (2015) and Samanta et al. (2015), we conducted an in-depth analysis of the NIRIS data to study whether variations in the high-resolution magnetic field correspond to PDs. From the NIRIS data, we could not identify magnetic flux cancellation events around the plumes' photospheric footpoints, which is considered as a signature of reconnection (e.g., Park 2020). Here, a flux cancellation event is defined as a converging motion of two opposite-polarity magnetic patches in the photosphere, accompanied by a decrease in the magnetic flux of both polarities. This is
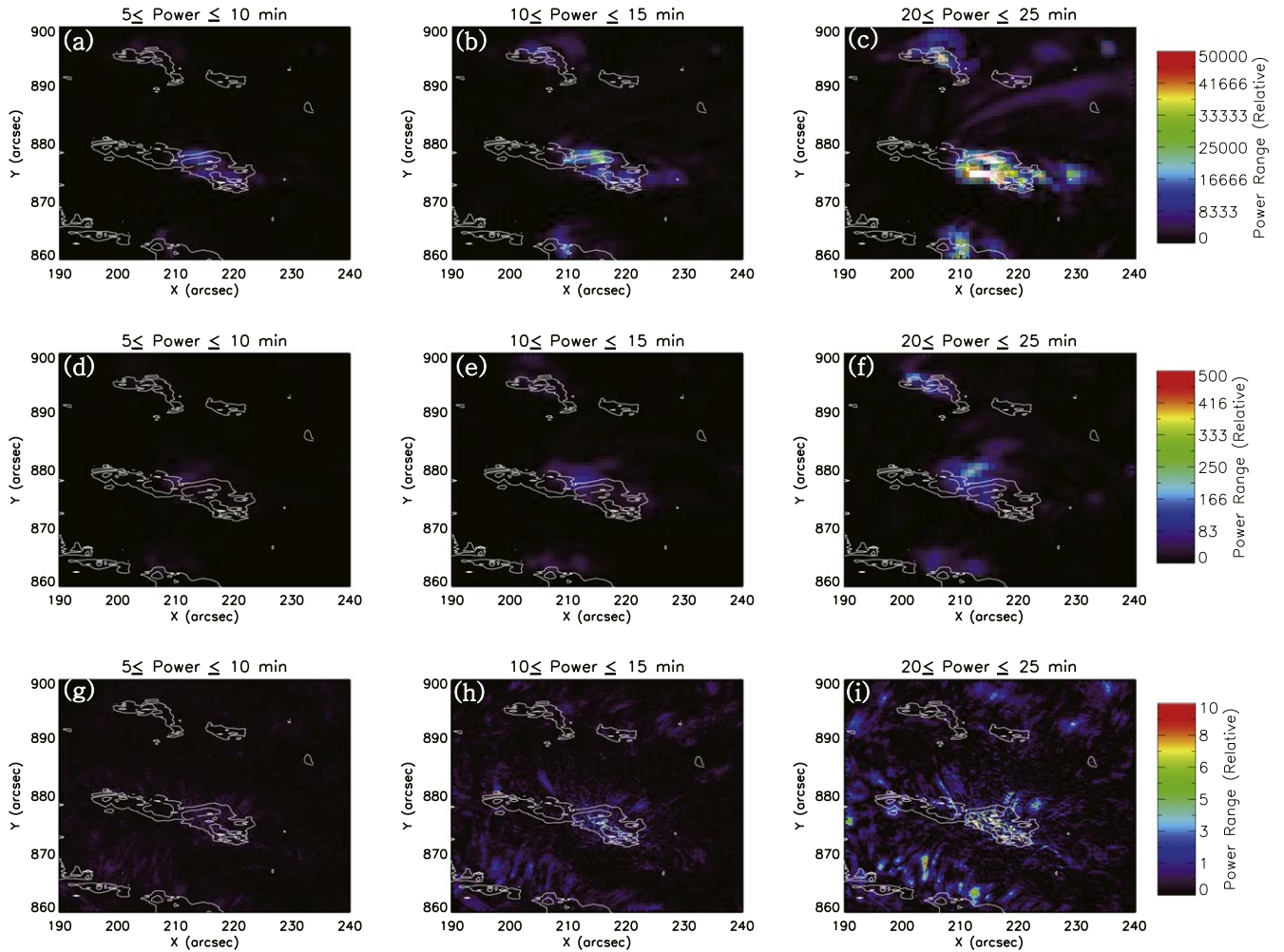
Figure 6. Power maps obtained by using SDO AIA 171 Å intensity (a)–(c), SDO AIA 304 Å intensity (d)–(f), and GST/VIS Hα± 0.8 Å (g)–(i) B–R asymmetry from 16:30 to 17:45 UT for three different period bands (5–10 minutes (a), (d), and (g), 10–15 minutes (b), (e), and (h), and 20—25 minutes (c), (f), and (i)). Type II spicules and plumes show their oscillation features in the long-period ranges. Color bars on the right side of the panel show the power range of VIS Hα± 0.8 Å, AIA 304 Å, and 171 Å periodicity, respectively. Contour denotes the brightness temperature.

because the region is inside the polar coronal hole, and the projection affects the magnetograms. Furthermore, we analyzed the AIA observations and found quasiperiodic heating (in the 304 Å channel) and associated outflows/jets at the plumes' bases. As seen in Figure 8 and the accompanying animation, the AIA 171/193 channels show PDs associated with recurrent footpoint heating in the 304 channels. In addition, we detected a moving magnetic feature (MMF) of mixed polarity from the NIRIS data at the footpoint of the plume (Figure 2(d) and accompanying animation). We speculate that the MMF can help in the build-up of magnetic energy in a tiny null-point topology (e.g., Wyper et al. 2018). As per MHD simulations and recent observations, quasiperiodic interchange reconnection at a null point may be modulated by photospheric/chromospheric slow-mode waves (e.g., Heggland et al. 2009; Kumar et al. 2022). It should be noted that for the onset of quasiperiodic reconnection, there is no need for repeated emergence of opposite/minority polarity (every 15–20 minutes) at the base of the plume. The repetitive reconnection generally persists in preexisting tiny BPs associated with minority polarities until its disappearance/decay (e.g., Kumar et al. 2019, 2022). Samanta et al. (2019) also showed similar results using IRIS and AIA observations. The cool material

generally falls back while the warm plasma and PDs propagate further along the plume. However, these studies do not discuss the origin of type II spicules.

4. Summary and Discussion

We analyzed multiwavelength images of a plume and a CBP at its base using GST, SDO, and IRIS observations. The plume originates at the edge of positive flux (majority polarity) surrounded by small magnetic patches with mixed polarities (positive and negative). We found a high Tb structure at the base of the plume located at the left side of the strong positive polarity. The heating at the base of the plume is likely associated with interchange reconnection between closed and open flux. The NIRIS magnetograms reveal evidence of mixed polarities at the base of the plume. In addition, GST Hα observations reveal the quasiperiodic occurrence of type II spicules ($P \approx$ 10–20 minutes) at the footpoint of the plume. We found that the type II spicules are rooted at the high Tb region "1." From the IRIS Mg II observation, we also found that the low-altitude upflows originated from the high Tb region where the type II spicules and the plumes are associated. From the VIS pseudo-Dopplergrams, we identified a repetitive occurrence of the type II spicules and producing plasma injections
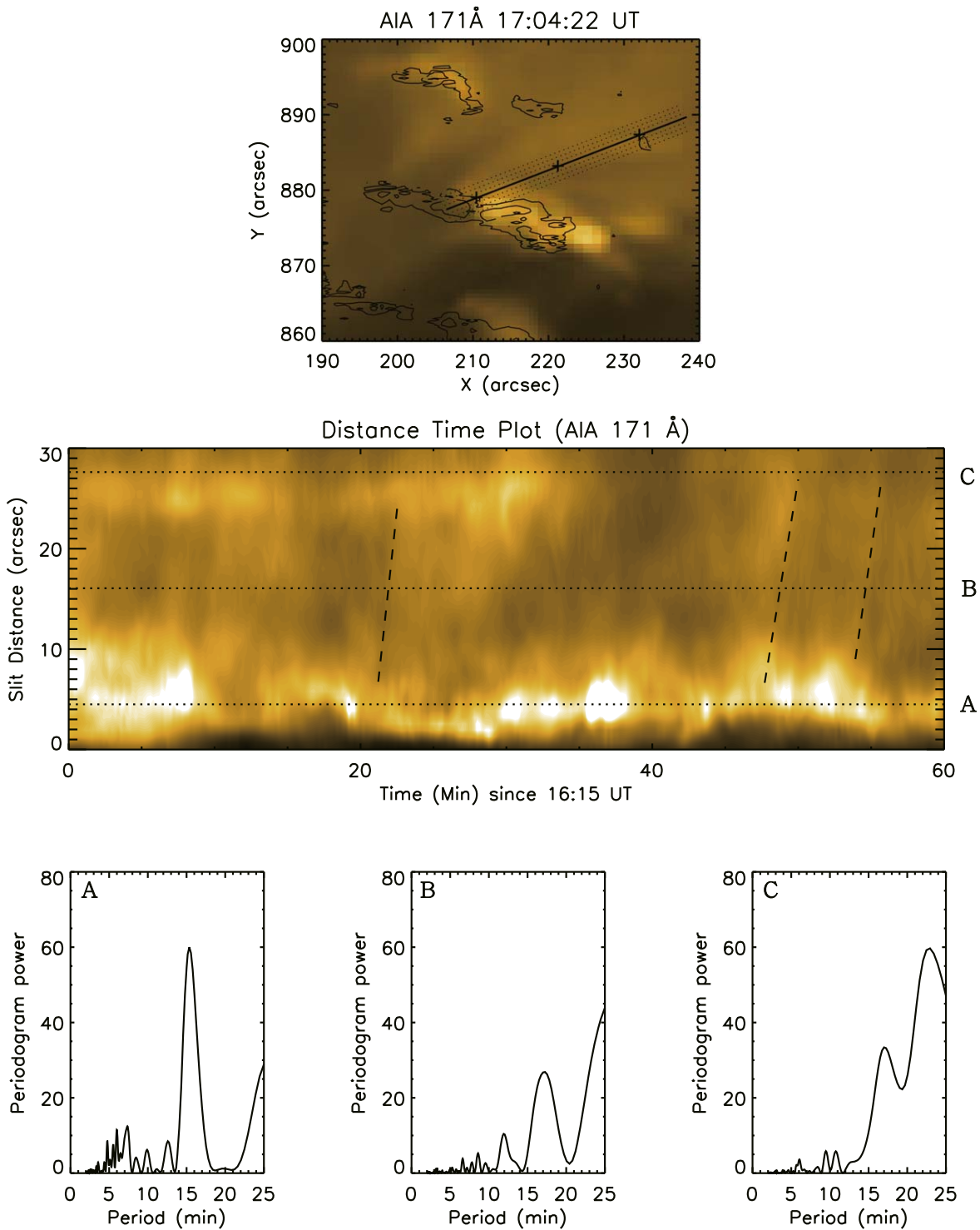
Figure 7. Top: AIA 171 Å intensity image with slit position along the plume. Contours indicate the brightness temperature. Middle: TD intensity plot along the slit in the top panel showing repetitive brightenings at the base of the plume and associated PDs. Horizontal and slanted dotted lines are used to archive typical power spectra and propagation speed of the PDs, respectively. Bottom: typical power spectra at the distance marked with the dotted lines in the middle panels.

and PDs at the base of the plume. We found the spicule and plume association by comparing the periods of PDs from AIA 171 Å intensity and the type II spicules occurrence in the ± 0.8 Å band of Hα. It is also noted that the occurrences of spicules and PDs in plumes have enhanced spectral power at the same period range, which means that they are highly coupled. It is likely that the repetitive upflow of the type II spicules may inject heated chromospheric material into the

corona and produce the PDs in the plume. Another option is that slow magnetoacoustic waves produced in a chromospheric slow magnetoacoustic resonator (e.g., Botha et al. 2011) result in the observed PDs and also the spicules. The latter could be made by a periodically induced magnetic reconnection, proposed by Chen & Priest (2006).

Previous observations have shown a possible connection between type II spicules and PDs ($P > 10$ minutes) in plumes
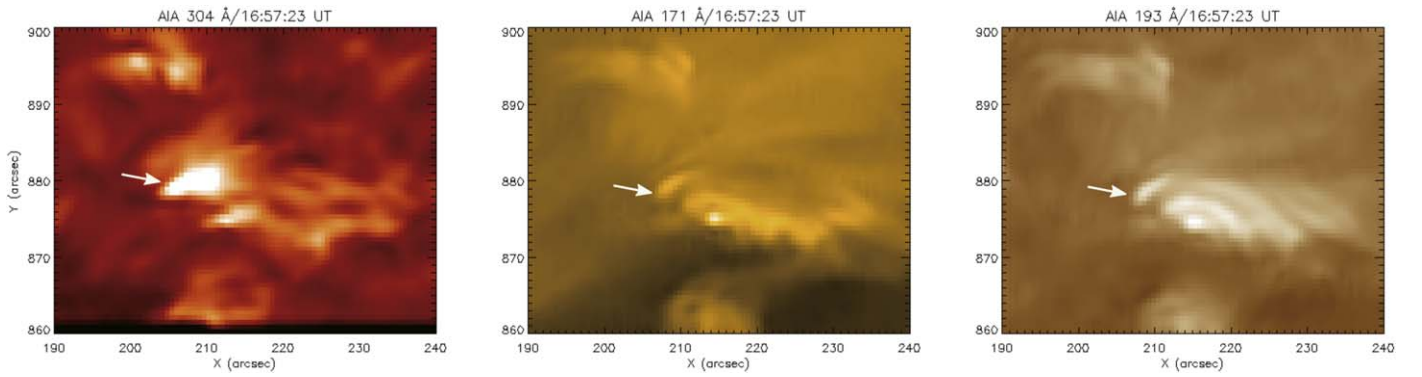
Figure 8. AIA images at 304 (left), 171 (middle), and 193 (right) Å that show recurrent outflows/jets and brightenings at the base of the plume. An arrow indicates the base of the plume where quasiperiodic reconnections occur. An animation of this figure is available. The animation runs from 15:01:35 to 17:57:11 UT and has a real-time duration of 22 s.

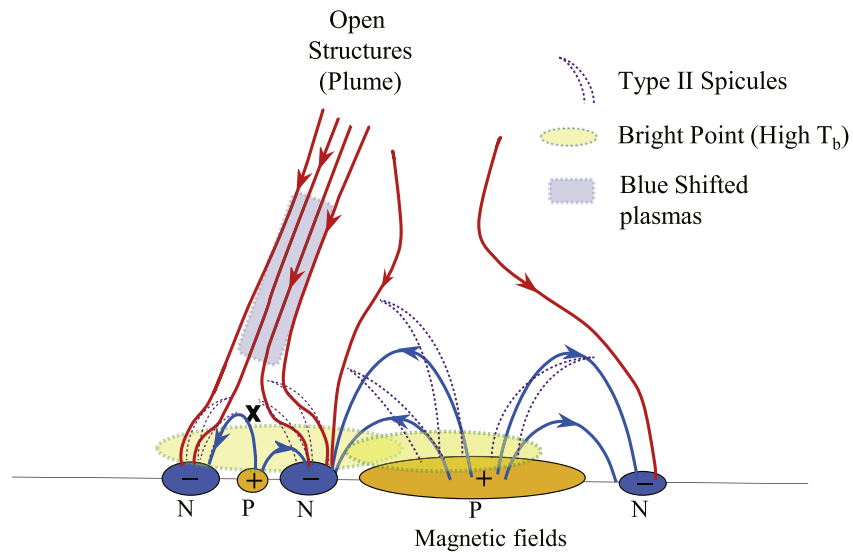(An animation of this figure is available.)

Figure 9. Schematic drawing of the magnetic field configuration of the central positive magnetic flux and the surrounding mixed polarity patches in the CH. The green oval represents the region of enhanced brightness temperature.

(Jiao et al. 2015; Samanta et al. 2015) using limb observations (AIA/IRIS) and concluded that type II spicules are the primary source of PDs. However, these studies do not investigate the activities related to magnetic reconnection at the base of the plume. Recent discoveries of short-period PDs/jetlets ($P\approx$ 5 minutes, in the band of p-modes) but also with the chromospheric slow magnetoacoustic resonance in plumes have revealed evidence for quasiperiodic reconnection in the tiny null-point topologies at the base of the plumes (Uritsky et al. 2021; Kumar et al. 2022). The quasiperiodic reconnection at the base of the plume could be triggered by a p-mode wave at the stressed null point or a slow wave leaking from the chromospheric resonator or produced at the acoustic cutoff, which produces jetlets (or type II spicules in AIA 304 Å) and PDs along the plume. The HMI magnetograms are incapable of detecting the minority polarities involved in the interchange reconnection at the base of the plumes (e.g., Wang 2016; Kumar et al. 2022). The high-resolution NIRIS magnetograms, however, are capable of detecting the minority polarities (e.g., Samanta et al. 2019). Recently, a statistical study by Qi et al. (2022) reported that spicules occurring at the footpoints of coronal plumes tend to be more dynamic (higher and faster).

Equally, spicules associated with PDs are usually faster than 50 km s^{-1}. The authors suggested a close association among spicule-like features in the chromosphere, transition region network jets, and ray-like features (plumes) in the corona. Here, we have shown evidence of repetitive brightenings/heating and blueshifted plasma (type II spicules) above the mixed polarities at the base of the plume. These activities support the idea of interchange reconnection between closed and open flux (rooted in the mixed polarities at the plume's footpoint) that produces the type II spicules (or jetlets) and long-period (>20 minutes) PDs along the plume. Actually, the broad range of the detected periods makes the interpretation in terms of the chromospheric resonator more realistic, as the resonant periods may be rather different for different inclinations of the magnetic field (e.g., Yuan et al. 2014).

Based on the observations, we propose a scenario (Figure 9) to support our interpretation of the relationship between the high Tb regions, type II spicules, and plumes. The type II spicules likely occurred at the high-temperature area (the CBP) near the edge of positive polarity surrounded by mixed polarity patches. The periodic occurrence of the spicules injects a heated chromospheric plasma from the chromosphere to the

corona along the open field lines (plume). This injection can produce slow magnetoacoustic waves and flows along the plume.

One may have concerns regarding the connection between spicules and PDs. From the described observations in Figures 2 and 3, the orientations of spicules are clearly different from those of the PDs. The difference is not surprising because they are related to the magnetic field configuration that connects the chromosphere and the corona, as depicted in the sketch of Figure 9.

There are no strong upflows on the right side of Tb region "2" in the chromospheric line (Mg II k2) data and no significant photospheric magnetic flux change in this region. Therefore, we believe that it does not significantly contribute to the plume. However, large CBPs can help in adding open flux to the plume via interchange reconnection, as proposed by Wang (1998). Based on this, we speculate that these upflows seen in Figures 4(e) and (h) may be produced from the upper chromosphere or transition region via interchange reconnection between the closed and open flux of the CBP.

Our high-resolution observations of the chromosphere, transition region, and corona by using GST, IRIS, and SDO lead us to conclude that type II spicules are the main source of plumes that provide continuous injecting plasma from the chromosphere along the plume. However, high-resolution coordinated observations with new instruments (e.g., DKIST, SolO) are required in the future to shed more light on the direct connection between type II spicules (jets) and plumes.

ORCID iDs

Kyung-Suk Cho ⬤ https://orcid.org/0000-0003-2161-9606
Pankaj Kumar ⬤ https://orcid.org/0000-0001-6289-7341
Il-Hyun Cho ⬤ https://orcid.org/0000-0001-7514-8171
Maria S. Madjarska ⬤ https://orcid.org/0000-0001-9806-2485
Valery M. Nakariakov ⬤ https://orcid.org/0000-0001-6423-8286
Eun-Kyung Lim ⬤ https://orcid.org/0000-0002-7358-9827
Wenda Cao ⬤ https://orcid.org/0000-0003-2427-6047
Vasyl Yurchyshyn ⬤ https://orcid.org/0000-0001-9982-2175

Xu Yang ⬤ https://orcid.org/0000-0002-3238-0779
Sung-Hong Park ⬤ https://orcid.org/0000-0001-9149-6547

References

Antonucci, E., Noci, G., Kohl, J. L., et al. 1997, in ASP Conf. Ser. 118, 1st Advances in Solar Physics Euroconference: Advances in Physics of Sunspots, ed. B. Schmieder, J. C. del Toro Iniesta, & M. Vazquez (San Francisco, CA: ASP), 273
Banerjee, D., Gupta, G. R., & Teriaca, L. 2011, SSRv, 158, 267
Botha, G. J. J., Arber, T. D., Nakariakov, V. M., et al. 2011, ApJ, 728, 84
Cao, W., Goode, P. R., Ahn, K., et al. 2012, in ASP Conf. Ser. 463, Second ATST-EAST Meeting: Magnetic Fields from the Photosphere to the Corona, ed. T. Rimmele (San Francisco, CA: ASP), 291
Cao, W., Gorceix, N., Coulter, R., et al. 2010a, AN, 331, 636
Cao, W., Gorceix, N., Coulter, R., et al. 2010b, Proc. SPIE, 7733, 773330
Chen, P. F., & Priest, E. R. 2006, SoPh, 238, 313
Cho, K.-S., Cho, I.-H., Madjarska, M. S., et al. 2021, ApJ, 909, 202
de Pontieu, B., McIntosh, S., Hansteen, V. H., et al. 2007, PASJ, 59, S655
De Pontieu, B., Title, A. M., Lemen, J. R., et al. 2014, SoPh, 289, 2733
DeForest, C. E. 2017, ApJ, 838, 155
DeForest, C. E., & Gurman, J. B. 1998, ApJL, 501, L217
DeForest, C. E., Plunkett, S. P., & Andrews, M. D. 2001, ApJ, 546, 569
Del Zanna, G., Bromage, B. J. I., & Mason, H. E. 2003, A&A, 398, 743
Gošić, M., Bellot Rubio, L. R., del Toro Iniesta, J. C., et al. 2016, ApJ, 820, 35
Heggland, L., De Pontieu, B., & Hansteen, V. H. 2009, ApJ, 702, 1
Horne, J. H., & Baliunas, S. L. 1986, ApJ, 302, 757
Jiao, F., Xia, L., Li, B., et al. 2015, ApJL, 809, L17
Kosugi, T., Matsuzaki, K., Sakao, T., et al. 2007, SoPh, 243, 3
Kumar, P., Karpen, J. T., Antiochos, S. K., et al. 2019, ApJ, 873, 93
Kumar, P., Karpen, J. T., Uritsky, V. M., et al. 2022, ApJ, 933, 21
Lamy, P., Liebaria, A., Koutchmy, S., et al. 1997, in Fifth SOHO Workshop: The Corona and Solar Wind Near Minimum Activity, ed. A. Wilson, 487
Leenaarts, J., Pereira, T. M. D., Carlsson, M., et al. 2013, ApJ, 772, 89
Leenaarts, J., Pereira, T. M. D., Carlsson, M., et al. 2013, ApJ, 772, 90
Lemen, J. R., Title, A. M., Akin, D. J., et al. 2012, SoPh, 275, 17
Madjarska, M. S. 2019, LRSP, 16, 2
Martínez-Sykora, J., De Pontieu, B., Hansteen, V. H., et al. 2017, Sci, 356, 1269
Nakariakov, V. M. 2006, RSPTA, 364, 473
Nakariakov, V. M., & King, D. B. 2007, SoPh, 241, 397
Park, S.-H. 2020, ApJ, 897, 49
Pereira, T. M. D., Leenaarts, J., De Pontieu, B., et al. 2013, ApJ, 778, 143
Pesnell, W. D., Thompson, B. J., & Chamberlin, P. C. 2012, SoPh, 275, 3
Poletto, G. 2015, LRSP, 12, 7
Pucci, S., Poletto, G., Sterling, A. C., et al. 2014, ApJ, 793, 86
Qi, Y., Huang, Z., Xia, L., et al. 2022, A&A, 657, A118
Raouafi, N.-E., Harvey, J. W., & Solanki, S. K. 2007, ApJ, 658, 643
Raouafi, N.-E., & Stenborg, G. 2014, ApJ, 787, 118
Rouppe van der Voort, L., Leenaarts, J., de Pontieu, B., et al. 2009, ApJ, 705, 272
Samanta, T., Pant, V., & Banerjee, D. 2015, ApJL, 815, L16
Samanta, T., Tian, H., Yurchyshyn, V., et al. 2019, Sci, 366, 890
Scargle, J. D. 1982, ApJ, 263, 835
Shumko, S., Gorceix, N., Choi, S., et al. 2014, Proc. SPIE, 9148, 914835
Sterling, A. C. 2000, SoPh, 196, 79
Tian, H., McIntosh, S. W., Habbal, S. R., et al. 2011, ApJ, 736, 130
Tian, H., Samanta, T., & Zhang, J. 2018, GSL, 5, 4
Uritsky, V. M., DeForest, C. E., Karpen, J. T., et al. 2021, ApJ, 907, 1
Wang, Y.-M. 1998, ApJL, 501, L145
Wang, Y.-M. 2016, ApJL, 820, L13
Wang, Y.-M., & Sheeley, N. R. 1995, ApJ, 452, 457
Withbroe, G. L., Feldman, W. C., & Ahluwalia, H. S. 1991, Solar Interior and Atmosphere (Tucson, AZ: Univ. Arizona Press), 1087
Wöger, F., von der Lühe, O., & Reardon, K. 2008, A&A, 488, 375
Wyper, P. F., DeVore, C. R., Karpen, J. T., et al. 2018, ApJ, 864, 165
Yang, X., Cao, W., & Yurchyshyn, V. 2022, ApJS, 262, 55
Yuan, D., Sych, R., Reznikova, V. E., et al. 2014, A&A, 561, A19
Yurchyshyn, V., Cao, W., Abramenko, V., et al. 2020, ApJL, 891, L21